Photoluminescent Self-Healable Nanocomposite of Waterborne Polyurethane and Sulphur and Molybdenum Co-Doped Graphitic Carbon Nitride Nanohybrid

Highlights

This chapter demonstrates the preparation of sulphur and molybdenum co-doped graphitic carbon nitride (g-C_3N_4) (Mo@S-CN) nanohybrid and the fabrication of self-healing water borne polyurethane (SHWPU)/Mo@S-CN (SHWPU/NS) nanocomposites for advanced applications. Mo@S-CN is an intriguing combination of g-C_3N_4 nanosheets and molybdenum oxide (MoO_x) nanorods, forming a complex lamellar structure. This unique arrangement significantly improves the inborn properties of SHWPU to an impressive degree, especially, mechanical strength, fracture toughness, and thermal stability, and introduces fluorescence activity into the matrix. Remarkably, fluorescence activity is developed because of electronic excitations occurring within the repeating polymeric tris-triazine units of Mo@S-CN nanohybrid. This fascinating feature was effectively harnessed by assessing the usability of aqueous dispersions of Mo@S-CN nanohybrid and photoluminescent SHWPU/NS nanocomposites as sustainable stains for bioimaging of human dermal fibroblasts (HDF) cells and as anti-counterfeiting materials, respectively. Most importantly, *in vitro* hemocompatibility assessment, *in vitro* cytocompatibility, cell proliferation assessment, and cellular morphology assessment, supported the biocompatibility nature of the Mo@S-CN nanohybrid and SHWPU/NS nanocomposites.

Parts of this chapter are preparing for publication.

Morang, S., Bandyopadhyay, A., Borah, N, Kar Annesha, Mandal, B. B., Mandal, M. and Karak, N. Photoluminescent self-healable waterborne polyurethane/Mo and S co-doped graphitic carbon nitride nanocomposite with bioimaging and encryption capability. (*Manuscript is under revision, ACS Applied Bio Materials, Manuscript ID: mt-2023-01259c*).

6.1. Introduction

The preceding three chapters delineate the tweaking of hard to soft domains of pristine waterborne polyurethane (WPU) through judicious molecular engineering. These chemical modifications result in substantial property improvements and the introduction of smart properties such as self-healing (SH), shape memory (SM), and so forth. Presently, medical science and other disciplines demand more captivating features e.g., photoluminescence behavior. At this juncture, graphitic carbon nitride (g-C_3N_4) emerges as a suitable choice for incorporating fluorescence attributes into SHWPU with incredible photo-catalytic activity [1]. However, g-C_3N_4 is associated with some flaws that restrict its application in superior applications, including, small specific surface areas, reduced quantum efficiency, rapid recombination of electron-hole pairs, limited response to visible light, etc. [2-4]. Literature advocates that elemental co-doping two or more elements into the g-C_3N_4 lattice is an effective way to improve the photocatalytic activity of g-C_3N_4 and increment in specific surface area, providing more active reaction sites. Additionally, transitional metals can form coordination complexes with various moieties present in a PU matrix, resulting in significant improvement in inborn properties and performance. For example, Wang et al. developed a bioinspired-PU by introducing reversible iron-catechol (DOPA-Fe^{3+}) cross-links and quadruple H-bonds bearing 2-ureido-4-[1H]-pyrimidinone (UPy) dimers as multifunctional blocks into a segmented PU backbone with carbamate/urethane linkages and semi-crystalline polycaprolactone (PCL) moieties [5]. They reported that the complexes formed by DOPA and Fe^{3+} were able to promote the crystallization of PCL, resulting in a substantial enhancement in Young's modulus and tensile strength. Again, counterfeiting has arisen as an emergent concern on a global scale for industries, governments, and consumers. The circulation of counterfeit paper currency not only results in major socioeconomic problems but also devalues genuiness of currency. Additionally, the production and distribution of counterfeit drugs pose severe health hazards, as they may have unknown or incorrect quantities of chemicals [6-8]. Therefore, anti-counterfeiting has grown into a decisive innovation for the protection of valuable and important objects that must not be fake, including currency, documents, certificates, brands, luxury goods, tickets, etc. [9].

In the present study, a series of photoluminescent self-healable WPU (SHWPU)/Mo@S-CN (SHWPU/NS) nanocomposites were prepared using sulphur and molybdenum co-doped g-C_3N_4 or Mo@S-CN nanohybrid as the reinforcing nanomaterials and other desired reactants. Interestingly, Mo@S-CN nanohybrid consists of g-C_3N_4 nanosheets and molybdenum oxide (MoO_x) nanorods that create a complex lamellar structure which not only triggered the properties upgradation (especially, mechanical

strength, fracture toughness, and thermal stability) but also imparted photoluminescence feature into SHWPU. Furthermore, *in vitro* hemocompatibility study, *in vitro* cytocompatibility, cell proliferation assessment, and cellular morphology assessment corroborated the biocompatibility nature of Mo@S-CN nanohybrid and SHWPU/NS nanocomposites. Leveraging its excellent biocompatibility and fluorescence properties, aqueous dispersions of Mo@S-CN nanohybrid were used for imaging human dermal fibroblasts (HDF) cells, and SHWPU/NS was employed as anti-counterfeiting materials.

6.2. Experimental

6.2.1. Materials

Starting materials used in the present study are isophorone diisocyanate (IPDI), poly(ε-caprolactone diol) (ε-PCL_{2000}), 2,2-bis(hydroxymethyl) propionic acid (DMPA), 2-aminophenyl disulfide (2-APDS), citric acid, glycerol, castor oil, triethyl amine (TEA), para-toluene sulphonic acid (*p*-TSA), calcium oxide (CaO), N, N-dimethylformamide (DMF), and dibutyltin dilaurate (DBTDL. All these materials have the same specifications as discussed in earlier chapters. Additionally, some other chemicals are also used as stated below.

Sodium molybdate dehydrate (SMD, Sigma Aldrich, USA) is a white, crystalline salt with a molecular weight of 241.95 $gmol^{-1}$ and a melting point of 100 ℃.

Guanidine hydrochloride (GuHCl, Sigma Aldrich, USA) is a crystalline salt soluble in water and alcohol. It has a molecular weight, density, and melting point of 95.53 $gmol^{-1}$, 1.35 gmL^{-1}, and 182.3 ℃.

2-Thiobarbituric acid (2-TBA, HiMedia, India) is an off-white to yellow powder and has a molecular weight of 144.15 $gmol^{-1}$ and a melting point of 245 ℃.

6.2.2. Methods

6.2.2.1. Preparation of monoglyceride of castor oil (MG_{CO})

In this study also, MG_{CO} was prepared from castor oil and glycerol as detailed in **Chapter 2**, **section 2.2.2.1**.

6.2.2.2. Preparation of glycerol ester of citric acid (GECA)

GECA was prepared from citric acid and glycerol as discussed in **Chapter 2**, **section 2.2.2.2**.

6.2.2.3. Preparation of S and Mo co-doped graphitic carbon nitride (g-C_3N_4) (Mo@S-CN) nanohybrid

A modified calcination method was adopted for preparing the targeted Mo@S-CN [10-11]. Firstly, the bulk S-doped g-C_3N_4 (S-CN) was prepared by polymerization of GuHCl and 2-TBA molecules under high temperature. In detail, 5 g of GuHCl and 0.05 g of 2-TBA were dissolved in a solution of 5 mL of distilled water and 5 mL of absolute ethanol. The solution was sonicated for 1 h and allowed to dry at 80 °C for 24 h to obtain a pink-colored product. In a muffle furnace, this product was calcined in a ceramic boat at 550 °C for 2 h under air with a heating rate of about 5 °C/min for both the heating and cooling processes. The obtained yellow powder was the bulk S-CN. Again, the bulk Mo@S-CN was prepared by further polymerization of bulk S-CN with SMD via the calcination condition. In detail, Mo@S-CN nanohybrid (a combination of nanorods and nanosheets) was developed by liquid exfoliation of as-prepared bulk Mo@S-CN in water. To exfoliate, a total weight of 50 mg of bulk Mo@S-CN powder was dispersed in 50 mL of water and sonicated for about 16 h. The remaining un-exfoliated and large-area nanohybrids were removed from the prepared suspension by centrifuge at about 3000 rpm. The resultant Mo@S-CN nanohybrid was used for further study.

6.2.2.4. Fabrication of SHWPU/NS nanocomposites

A series of SHWPU/NS nanocomposite emulsions were prepared via a combination of pre-polymerization and solution techniques with various amounts of Mo@S-CN nanohybrid. Initially, SHWPU dispersion was prepared by the pre-polymerization method as stated in previous chapters. Then, various weight percentages of Mo@S-CN (solid content of ~2 mg/mL) nanohybrid were mixed with the SHWPU dispersion at 70-80 °C under N_2 atmosphere for 4 h to obtain the targeted SHWPU/NS nanocomposite emulsions. Notably, in this present work, SHWPU is the same as SHWPU-3 of the previous chapter i.e., **Chapter 5**. Again, four compositions, namely, SHWPU/$NS_{0.01}$, SHWPU/$NS_{0.1}$, SHWPU/$NS_{0.5}$, and SHWPU/$NS_{1.5}$, were prepared with 0.01 wt%, 0.1 wt%, 0.5 wt%, and 1.5 wt% loading of Mo@S-CN nanohybrid with respect to total weight of SHWPU, respectively.

6.2.3 Characterization and tests

6.2.3.1. Structural characterization and property evaluation

A set of distinctive characterization techniques and tests were used to characterize and evaluate various properties of the Mo@S-CN nanohybrid, SHWPU/NS nanocomposite emulsions, and their films, as described in previous chapters. Additionally, morphology and elemental compositions were investigated using a scanning electron microscope (SEM, Model-JSM 6390LV, JEOL, Japan), and field emission scanning electron microscopy (FE-SEM, Model-JSM7200F, JEOL, Japan). X-ray photoelectron spectra (XPS) were acquired on an

ESCALAB Xi+ (ThermoFisher Scientific, USA) with Al Kα (hν = 1361 eV) as the excitation source. The Zetasizer Nano ZS90 (Malvern Instruments Ltd., UK) was used to measure the average size of the samples, their distributions, and zeta potential value. The UV-vis absorption experiments were carried out for bulk Mo@S-CN, Mo@S-CN-NS nanohybrid, and SHWPU/NS emulsion on a UV-Vis spectrophotometer (Model-Evolution 300, ThermoFisher Scientific, USA). The photoluminescence (PL) was performed by the FLUOROLOG-3-TAU fluorescence spectrometer. A portable WFH-204B ultraviolet lamp was utilized to radiate the image.

6.2.3.2. *In vitro* hemocompatibility study

In vitro, a hemocompatibility study of SHWPU/$NS_{1.5}$ discs and Mo@S-CN nanohybrid suspension-coated slides was performed according to previously defined protocols as stated in **Chapter 4** and **Chapter 5**.

6.2.3.3. *In vitro* cytocompatibility and cell proliferation study

The *in vitro* cytocompatibility and cell proliferation study of SHWPU/$NS_{1.5}$ discs and Mo@S-CN nanohybrid suspension-coated slides were inspected following the same protocol and methods as explained in **Chapter 4**, and **Chapter 5**.

6.2.3.4. Bioimaging and anti-counterfeiting test

For bio-imaging, Mo@S-CN nanohybrid aqueous dispersion was sterilized through UV exposure and mixed in a complete cell culture medium to reach a concentration of 3 mg/mL. HDFs were seeded and cultured for 48 h on glass coverslips in 6 well plates. Thereafter, Mo@S-CN nanohybrid containing media was added to the seeded cells and they were further incubated for 72 h. These live cells were thereafter examined under the excitation wavelengths of 365 nm, 470 nm, and 545 nm. The images were captured using an inverted fluorescence microscope (Axio observer, Zeiss, Germany) in all of these channels as well as bright-field for co-localization. This was used to evaluate the prospective fluorescence tagging of cells using Mo@S-CN nanohybrid. For the anti-counterfeiting test, an aqueous dispersion of SHWPU/$NS_{1.5}$ was used directly to write the "**APNL**" on a filter paper with a pore size of 20 μm. Then, allow drying for a few minutes inside a convection oven at 60°C. Finally, the filter paper was exposed to various wavelengths using a UV chamber, and digital photographs were captured using a mobile phone (Samsung Galaxy A50S).

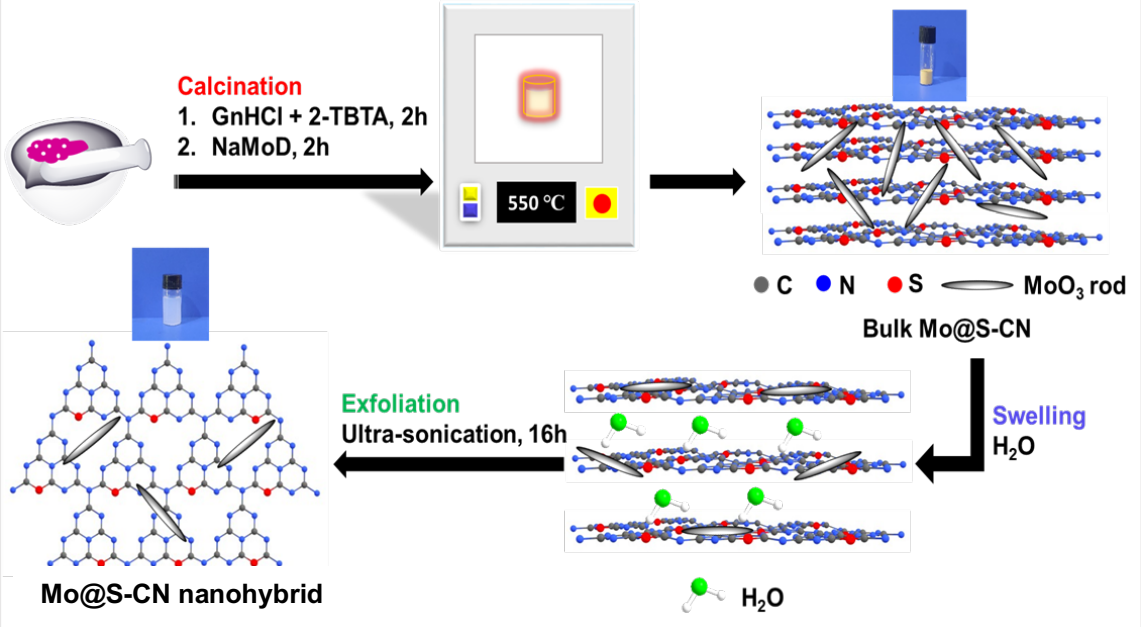

Scheme 6.1. Preparation of Mo@S-CN nanohybrid.

6.3. Results and discussion

6.3.1. Preparation and characterization of Mo@S-CN nanohybrid

The exfoliated Mo@S-CN nanohybrid was prepared from SMD, GuHCl, and 2-TBA by calcination as shown in **Scheme 6.1**. The morphology of the Mo@S-CN nanohybrid was evaluated using SEM, FESEM, and TEM analyses. As demonstrated in **Figure 6.1 (a)**, the Mo@S-CN nanohybrid has multiple layer-stacked structures with non-uniform sizes. The EDS element mapping and corresponding EDS spectrum are shown in **Figure 6.1. (b-g)** displayed that C, N, O, S, and Mo elements are dispersed on the nanomaterial. However, surprisingly, FESEM and TEM images (**Figure 6.1. (h-k)** unveiled that Mo@S-CN nanohybrid is composed of MoO_3 nanorods and g-C_3N_4 nanosheets, resulting in the formation of a heterojunction structure, which agrees with a previous work [10]. Additionally, Mo@S-CN nanohybrid aqueous dispersion is shown in **Figure 6.2 (a)** and it has an average particle size of 644.16 nm and an average zeta potential value of -30.27 mV, which supports its good colloidal stability. Profiting from the highly negative surface charge, the dispersion of Mo@S-CN nanohybrid is very stable, remaining free from aggregation even when left undisturbed for several months. To scrutinize the crystallinity of bulk S-CN, bulk Mo@S-CN, and Mo@S-CN nanohybrid, the P-XRD analysis was performed and the results are illustrated in **Figure 6.2. (b)**.

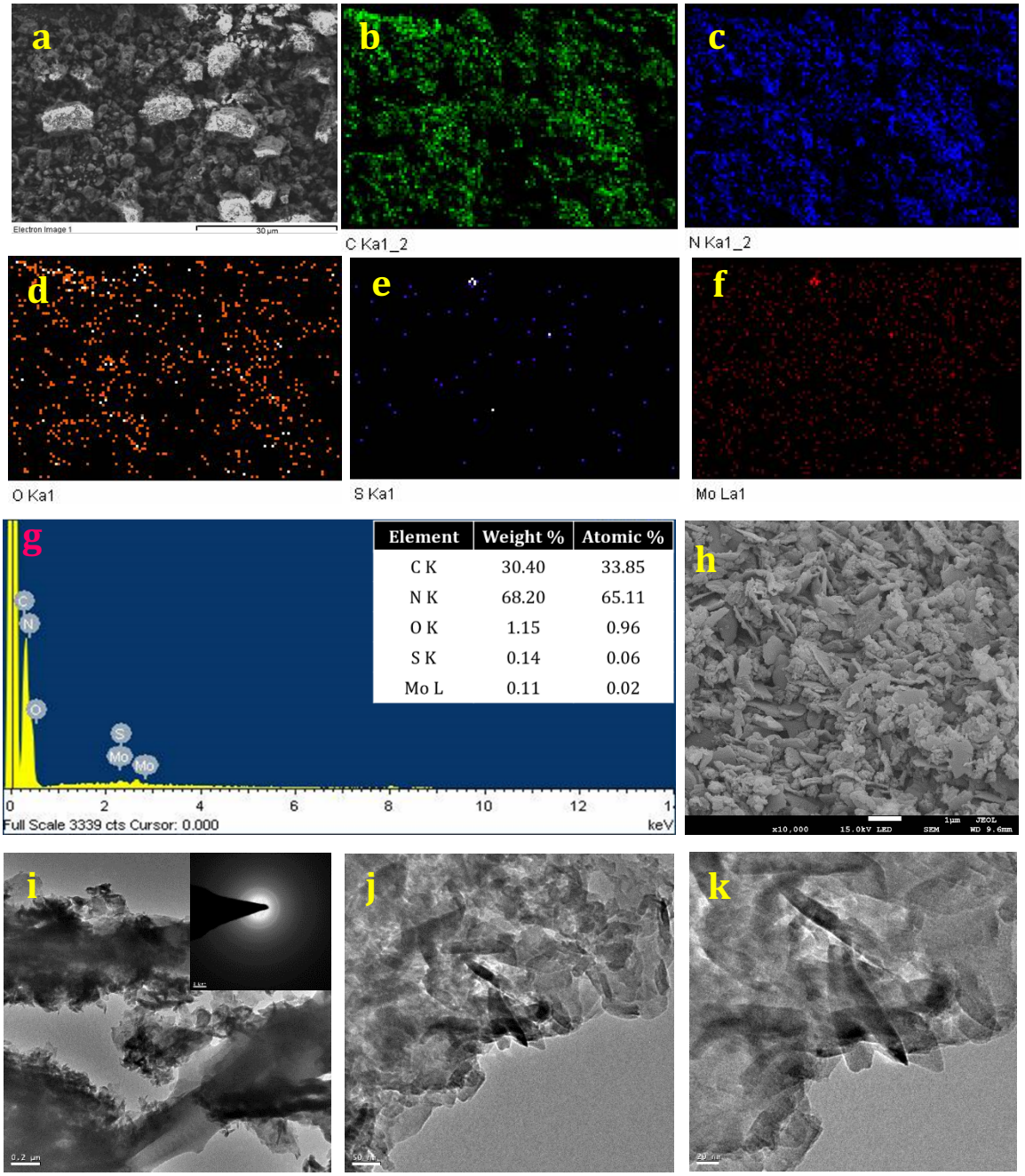

Figure 6.1. (a) SEM image, SEM (EDS) elemental mapping of (b) carbon, (c) nitrogen, (d) oxygen, (e) sulfur, and (f) molybdenum, (g) EDS spectrum, (h) FESEM image (scale: 1µm), TEM images at various scale (i) 200 nm; inset: SAED pattern, Size scale (j) 50 nm, and (k) 20 nm of Mo@S-CN nanohybrid.

It has been observed that the diffraction patterns of bulk S-CN and bulk Mo@S-CN with a strong peak near 2θ= 27.6°, corresponding to the interlayer stacking of aromatic segments (002) with an inter-planar distance d= 0.32 nm. Another small diffraction peak near 2θ= 13.3° was found which can be accredited to the in-plane repeated tri-s-triazine units (100) with a separation of d= 0.66 nm. However, in the case of Mo@S-CN nanohybrid, there was only one small peak of (002) was detected, indicating the proper exfoliation of bulk

Mo@S-CN via reducing interlayer forces. Similar observations were made in prior literature about g-C_3N_4-based nanomaterials [11-12].

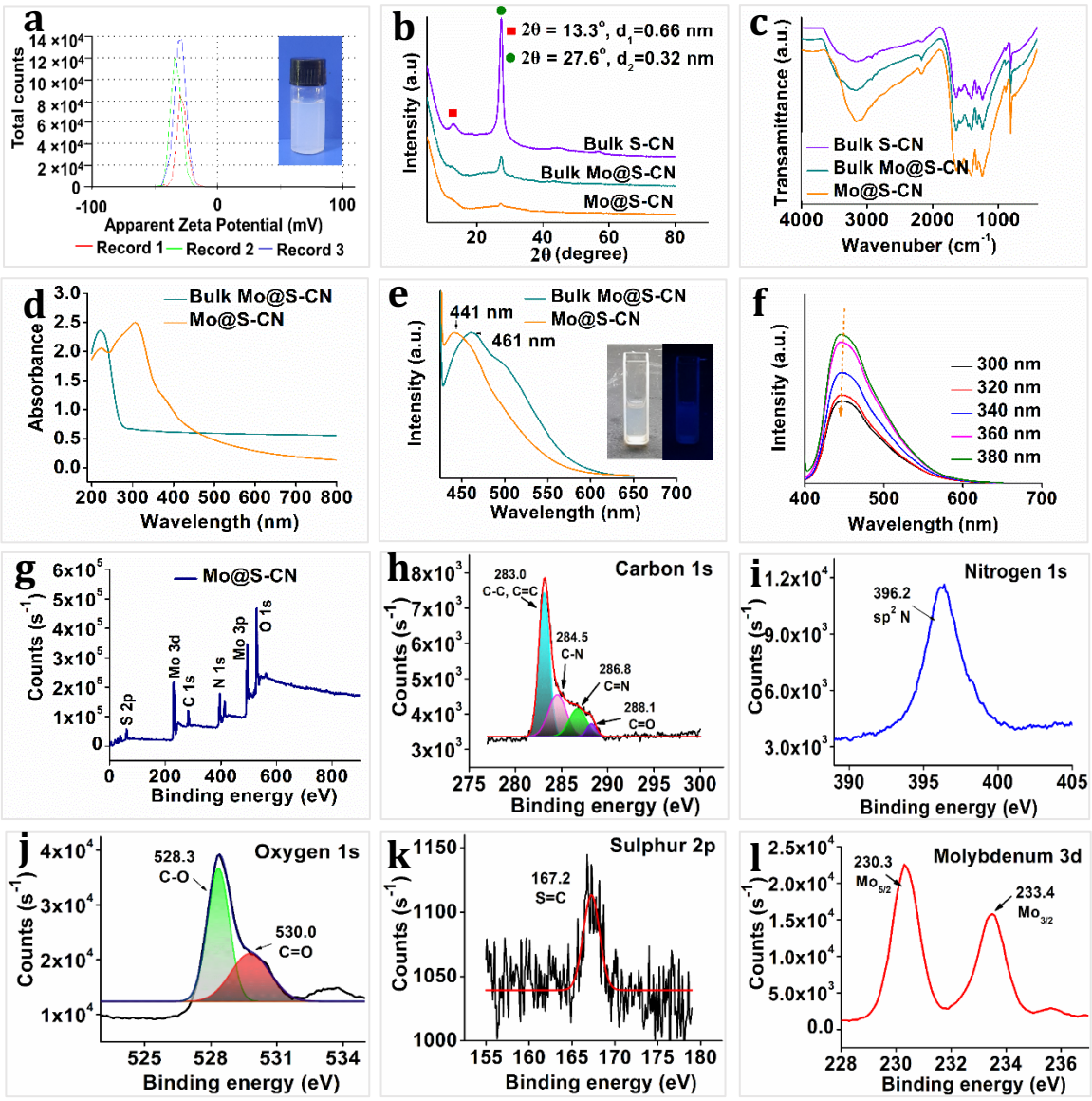

Figure 6.2. (a) Zeta Potential (mV), (b) P-XRD curves, (c) FTIR spectra, of bulk S-CN, bulk Mo@S-CN and Mo@S-CN nanohybrid, (d) UV-absorption spectra, (e) normalized PL spectra of bulk Mo@S-CN and Mo@S-CN nanohybrid, inset: the color change of exfoliated Mo@S-CN nanohybrid solution before and after UV-light (254 nm) illumination, (f) PL spectra of Mo@S-CN nanohybrid aqueous solution excited at a range of wavelength, (g) XPS survey spectrum of Mo@S-CN nanohybrid and high-resolution peak fitting spectra of (h) C 1s, (i) N 1s, (j) O 1s, (k) S 2p, and (l) Mo 3d.

The FTIR spectra of bulk S-CN, bulk Mo@S-CN, and Mo@S-CN nanohybrid are shown in **Figure 6.2. (c)**. A sharp characteristic peak at 808 cm^{-1} can be assigned to the triazine units. All peaks located in the range of 1242 cm^{-1} to 1650 cm^{-1} are attributed to the typical stretching vibrations of C–N of the heterocyclic rings. Again, broad peaks near 3172 cm^{-1} correspond to the –NH– or $–NH_2$ stretching vibrations of uncondensed amino groups and

surface-adsorbed −OH groups. Additionally, the peak at 2175 cm^{-1} can be ascribed to the vibration of CO_2 adsorbed on the surface of the nanomaterials. It is important to note that all samples (bulk and nanohybrid) exhibited identical vibrational band which indicate that there are no more functional groups emerged during the exfoliation process for the preparation of the targeted Mo@S-CN nanohybrid. The electronic structure of the Mo@S-CN nanohybrid was assessed from their UV absorption and PL spectra. As shown in **Figure 6.2. (d)**, absorption maximum (λ_{MAX}) of exfoliated Mo@S-CN nanohybrid displays a small blue shift in comparison with bulk Mo@S-CN, which might be because of the improved photoabsorption and photoresponsive nature [11]. PL spectra (**Figure 6.2. (e)**) of Mo@S-CN nanohybrid demonstrate a blue shift of ~20 nm compared with bulk Mo@S-CN which can be accredited to the quantum confinement effect with the conduction and valence band shifting in opposite directions. The aqueous dispersion Mo@S-CN nanohybrid emits blue PL under UV light (365 nm), as shown in the inset of **Figure 6.2. (e)**. Moreover, the PL spectra exhibit an insignificant redshift (all located in the blue light region) with an increase in excitation wavelength from 300 nm to 380 nm. Therefore, it can be acclaimed that Mo@S-CN nanohybrid has excitation wavelength-dependent PL characteristics because of optical selection effects arising from nanoparticles of varying sizes (quantum confinement effect) and the significant distribution of emissive trap sites on their surfaces [13-14]. Furthermore, XPS was employed to evaluate the elemental composition and valence states of the Mo@S-CN nanohybrid. As illustrated in **Figure 6.2. (g-l)**, the XPS survey spectrum of Mo@S-CN nanohybrid confirms the existence of C, N, O, S, and Mo elements. The C1 spectrum can be mainly divided into three peaks located at about 283.0 eV (C–C/ C=C), 284.5 eV (C–N), and 288.1 eV (C=O), which are straightforwardly associated with sp2-bonded carbon of Mo@S-CN nanohybrid. As shown in **Figure 6.2 (i)**, the N 1s spectrum shows a characteristic peak at 396.4 eV which can be accredited to the sp^2 hybridized C–N=C group. Two peaks at 528.3 (C–O) and 530.0 (C=O) correspond to the CO_2 adsorbed on the surface of Mo@S-CN nanohybrid which is also supported by FTIR data. The characteristic peak of S $2p_{3/2}$ was observed at 167.2 eV which can be attributed to the C=S formed in the Mo@S-CN nanohybrid lattice via substituting N atoms [9]. Furthermore, the Mo 3d spectrum shows two characteristic peaks at 230.3 eV ($Mo_{5/2}$ with +4 oxidation state) and 233.4 eV ($Mo_{3/2}$ with +6 oxidation state) because of oxidation of Mo in air, according to a previous report [15].

6.3.2. Fabrication and characterization of SHWPU/NS nanocomposites

As shown in **Scheme 6.2**, photoluminescent SHWPU/NS nanocomposites with improved thermo-mechanical properties were prepared by varying Mo@S-CN-NS nanohybrid amount from 0.01 wt% to 1.5 wt% with respect to SHWPU matrix.

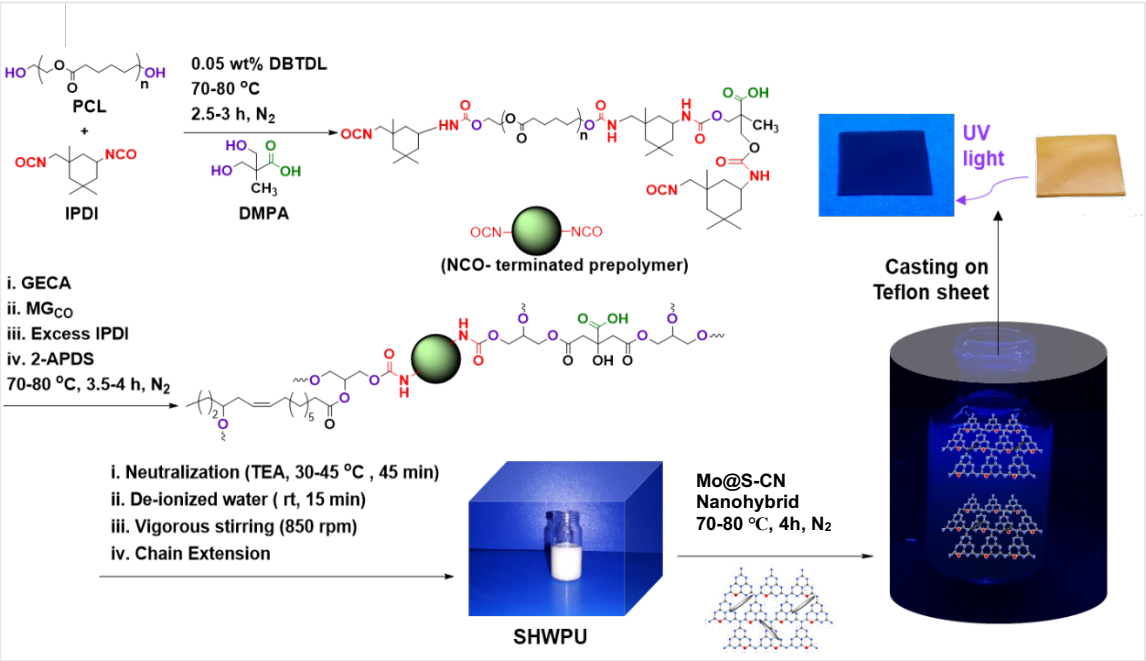

Scheme 6.2. Preparation of SHWPU/NS nanocomposite dispersion.

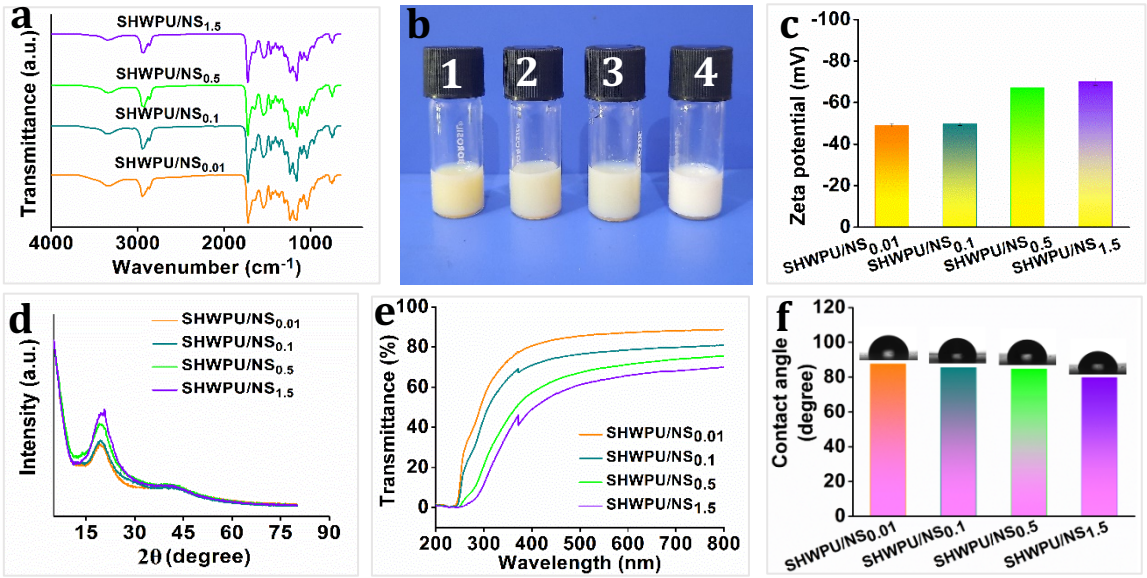

Figure 6.3. (a) FTIR spectra, (b:1-4) digital images for nanocomposite dispersions, (c) Zeta potential (mV), (d) P-XRD spectra, of SHWPU/NS nanocomposites, (e) the percentage of transmittance (thickness ~0.15 mm), and (f) water contact angle, of SHWPU/NS films.

A perusal of FTIR spectra of SHWPU/NS nanocomposites (**Figure 6.3 (a)**) demonstrated the absence of a vibrational peak near 2250-2270 cm^{-1} corresponding to the free –NCO group. This zero availability of –NCO group depicts their complete conversion into either urethane or urea groups of the SHWPU system [16]. As expected, the broad peak (near

3500 cm^{-1}) for the free -OH group was absent, but a broad peak was observed close to 3343 cm^{-1} which can be accredited to –NH stretching vibration. The characteristic peak associated with –NH bending vibration was found at 1463 cm^{-1}. Notably, two characteristic peaks located at 2930 cm^{-1} and 2862 cm^{-1} can be ascribed to asymmetric and symmetric stretching vibrations of $-CH_2$ groups, respectively. A medium peak spotted near 1370 cm^{-1} can be assigned to –CH bending vibration. Furthermore, the vibrational frequency for –C=O corresponding to carbamate and urea groups was noticed as 1729 cm^{-1} and 1643 cm^{-1}, respectively [17]. These findings unambiguously validate the creation of a urethane backbone. The aqueous dispersions of SHWPU/NS nanocomposite are milky white in appearance as shown in **Figure 6.3 (b)**. DLS study revealed that the average particle sizes and zeta potential values were in the range of SHWPU/$NS_{0.01}$, SHWPU/$NS_{0.1}$, SHWPU/$NS_{0.5}$, and SHWPU/$NS_{1.5}$, 72.74 nm, and -67.13 mV, 92.9 nm and -49.03 mV, 90.47 nm and -49.63 mV, 242.56 nm and -70.1 mV, respectively (**Figure 6.3 (c)**). Two factors that highly influence the particle size and colloidal stability of the nanocomposite dispersion are cross-linking density and emulsification [18]. Since all the nanocomposites were fabricated using the same SHWPU matrix i.e., the same amount of cross-linker and emulsifier present in each case, the average particle sizes are remarkably like each other. The P-XRD pattern of SHWPU/NS nanocomposite film was recorded in the range of 2θ of 5° to 80°, as shown in **Figure 6.3. (d)**. Previous study unveiled that the semi-crystalline ε-PCL_{2000} exhibits two characteristic peaks at 2θ= 21.4° and 23.8° corresponding to (110) and (200) reflection plans [19]. However, these peaks were not observed in the final products i.e., SHWPU/NS nanocomposite, instead a broad peak near 19.69° was detected. This change can be ascribed to the structural deformation caused by chemical cross-linking during polymerization. It is pertinent to note that peak intensity increases with an increase in Mo@S-CN nanohybrid content. However, no additional peaks associated with Mo@S-CN nanohybrid were observed potentially due to remarkably low loading of the same. The transparency of nanocomposite films with a thickness of ~0.15 mm was measured using a UV-visible spectrophotometer. As shown in **Figure 6.3 (e)**, the percentage of transmittance of SHWPU/$NS_{0.01}$, SHWPU/$NS_{0.1}$, SHWPU/$NS_{0.5}$, and SHWPU/$NS_{1.5}$, was 88.43%, 80.52%, 75.63%, and 69.55%, respectively. This trend of transparency can be referenced to the increase in the crystallinity in the nanocomposite films as the concentration of Mo@S-CN nanohybrid rises. Moreover, contact angles varied from 79.7° to 87.5° which confirms the hydrophilic nature of the developed nanocomposite films with a large number of polar groups (e.g., ester, urethane, etc.) on their surface.

6.3.3. Thermal analysis of SHWPU/NS nanocomposite films

The thermal stability of the SHWPU/NS nanocomposite films was evaluated and compared with the pristine SHWPU using a TGA machine. The findings are depicted in **Figure 6.4** and summarized in **Table 6.1**.

Table 6.1. The thermal parameters of SHWPU/NS nanocomposite films derived from TGA and DSC analyses.

Sample Code	T_1 (℃)	T_{MAX} (℃)	T_2 (℃)
SHWPU/$NS_{0.01}$	254.8	340.1	434.2
SHWPU/$NS_{0.1}$	255.2	341.5	434.6
SHWPU/$NS_{0.5}$	256.9	343.1	434.7
SHWPU/$NS_{1.5}$	257.8	348.0	435.9
*SHWPU	249.9	322.9	433.5

*Reproduced from **Chapter 5** for better understanding.

As discussed in the previous chapters, the thermal properties of a polymeric material depend on numerous factors including, structural rigidity (e.g., benzene ring), molecular weight, chemical and physical cross-linking, nanomaterial nature and loading percentage, etc. [20]. Like previous results of thermal studies, three major thermal degradations were observed for all SHWPU/NS nanocomposite films as shown in **Figure 6.4. (a)** and **(b)**. The initiation of thermal disintegration (T_1) of various thermo-labile moieties (e.g., long aliphatic chains of MG_{CO}) was seen in the range of 254.8 ℃ to 257.8 ℃. The second step degradation (T_{MAX}) i.e. maximum weight was detected in between 340.1 ℃ and 348 ℃ which can be ascribed to thermal degradation of prime groups such as urethane, ester, urea, etc. [21]. Again, the final step (T_2) was noticed near 434 ℃ corresponding to the deterioration of the most thermo-stable moieties e.g., the benzene ring of 2-APDS, and the cycloaliphatic ring of IPDA and IPDI, heterocyclic rings of Mo@S-CN nanohybrid, which are turned into char. Remarkably, a simple inspection of the TGA and DTG curves disclosed that there was a substantial increment (more than 20 ℃) in the T_{MAX} after incorporating Mo@S-CN nanohybrid into the SHWPU matrix and the increment was dose-dependent of nanomaterial. As mentioned in **Chapter 1**, g-C_3N_4 exhibits eye-catching properties including excellent thermal stability due to polymeric triazine rings

[22]. So, the rigid heat-resistant core structure Mo@S-CN nanohybrid imparts a stabilizing effect into SHWPU by absorbing the thermal energy and hence constraining the thermal movement of the polymer chains [23]. Additionally, Mo@S-CN nanohybrid also serves as a physical barrier, preventing the volatile groups from escaping the polymeric system and thereby delaying thermal decomposition.

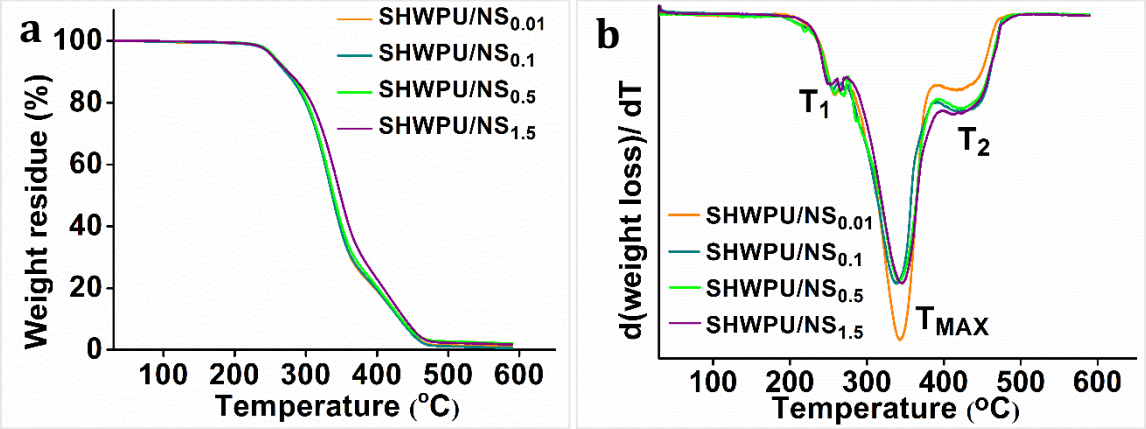

Figure 6.4. (a) TGA thermograms and (b) DTG curves of SHWPU/NS nanocomposite films.

6.3.4. Mechanical properties of SHWPU/NS nanocomposite films

According to the results collected from stress-strain profiles (**Figure 6.5 (a)** and **Table 6.2**), all SHWPU/NS nanocomposite films exhibited outstanding comprehensive mechanical performance. As shown in **Figure 6.5 (a)** and **(b)**, the tensile strength and percentage of strain at break were determined to be 28.37±1.04 MPa and 1670±97% for SHWPU/$NS_{0.01}$, 29.23±1.37 MPa and 1465±111% for SHWPU/$NS_{0.1}$, 30.89±1.76 MPa and 1370±87% for SHWPU/$NS_{0.5}$, 34.11±2.11 and 1085±81% for SHWPU/$NS_{1.5}$, respectively. Notably, SHWPU/$NS_{1.5}$ film has a tensile strength of 1.39 times greater than that of pristine SHWPU, as discussed in **Chapter 5**. Meanwhile, toughness was also increased significantly and the values varied from 198.2 MJm^{-3} to 230.3 MJm^{-3}, as illustrated in **Figure 6.5 (b)**. Extraordinarily, a sample film of SHWPU/$NS_{0.5}$ (weighing 0.283 g and measuring 60 mm in length, 5 mm in width, and 0.68 mm in thickness) showed no damage even when subjected to lift a 15 kg dumbbell, which is 53,003 times heavier than the film itself. As discussed in the preceding chapters, mechanical performance is highly influenced by several factors such as size, structure, loading as well as homogeneous dispersion of the nanomaterial, molecular weight of the hard and soft segments, crystallinity, chain entanglement, physico-chemical cross-linking, the orientation of segments, hydrogen bonding, π-π interactions between the hard and soft segments, etc. [24].

Table 6.2. Mechanical properties of the SHWPU/NS nanocomposite films.

Sample Code	Tensile strength (MPa)	Strain (%)	Toughness (MJm^{-3})	Fracture energy (MJm^{-2})
$SHWPU/NS_{0.01}$	28.37±1.04	1670±97%	230.3	73.65±1.47
$SHWPU/NS_{0.1}$	29.23±1.37	1465±111	207.2	77.85±1.63
$SHWPU/NS_{0.5}$	30.89±1.76	1370±87%	221.0	123.5±3.33
$SHWPU/NS_{1.5}$	34.11±2.11	1085±81%	198.2	140.98±4.65
*SHWPU	24.56±1.3	1755±144	212.7	46.74±1.02

*Reproduced from **Chapter 5** for better understanding.

It has been observed that tensile strength gradually increases as the content of Mo@S-CN nanohybrid arises. In the current investigation the preferentially aligned lamellar structured Mo@S-CN nanohybrid with high surface area, high aspect ratio, and high rigidity (polymeric heterocyclic rings, namely, triazine rings), acts as a strong reinforcing agent for the SHWPU matrix. The inclusion of this nanohybrid leads to a reduction in the overall free volume of the pure SHWPU matrix, resulting in enhanced mechanical strength of the material [25-26]. Notably, other factors such as the four wings of GECA, the asymmetric repeating units of IPDA-IPDI, the rigid structure of 2-APDS, and strain-hardening characteristics also contribute positively to the increase in mechanical strength, as mentioned in the previous chapter. As expected, the strain (%) at break was decreased from 1670±97% to 1085±81% with an increase in Mo@S-CN nanohybrid loading from 0.01 wt% to 1.5 wt% because of restriction in the chain movement after the nanocomposite fabrication. Furthermore, the fracture energies (**Figure 6.5 (d-f)**) of $SHWPU/NS_{0.01}$, $SHWPU/NS_{0.1}$, $SHWPU/NS_{0.5}$, and $SHWPU/NS_{1.5}$ were measured to be 73.65±1.47 MJm^{-2}, 77.85±1.63 MJm^{-2}, 123.5±3.33 MJm^{-2}, and 140.98±4.65 MJm^{-2}, respectively, using Greensmith's method [27]. The superior fracture energy exhibited by these nanocomposite films can be accredited to the synergistic effects of their optimized structure and the robust interfacial non-covalent interactions, e.g., hydrogen bonds and π-π interactions. These interactions effectively impede crack propagation, mitigating local stress concentration around the crack tip.

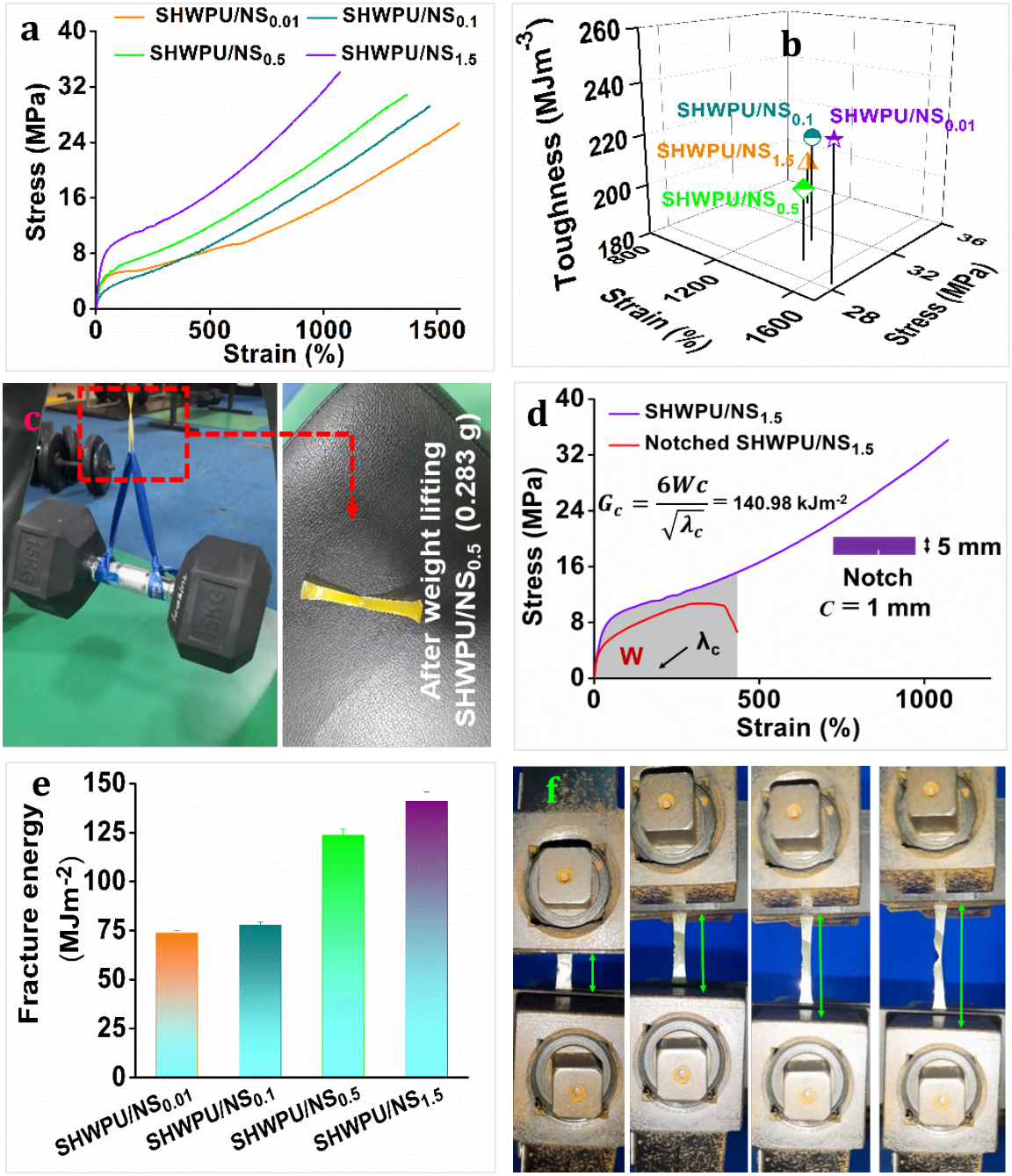

Figure 6.5. (a) Stress-strain profiles, (b) toughness (MJm^{-3}), of SHWPU/NS nanocomposite films, (c) weightlifting test by using SHWPU/$NS_{0.5}$ film, (d) stress-strain curves of un-notched and notched SHWPU/$NS_{1.5}$ film, (e) fracture energies (MJm^{-2}), and (f) representative digital photos of fracture test on SHWPU/$NS_{1.5}$ film.

6.3.5. Self-healing performance of SHWPU/NS nanocomposite films

As discussed in the previous chapters, the SH ability of polymers is positively associated with the molecular chain dynamics and it required sufficient local diffusion of polymeric chains across the fractured interfaces to facilitate the healing process [28]. Each SHWPU/NS nanocomposite consists of dual dynamic interactions, namely, dynamic disulfide

bonds originating from 2-APDS moieties and non-covalent interactions existed between two carbamate groups, two urea groups, carbamate-urea groups, as shown in **Figure 6.6 (a)**.

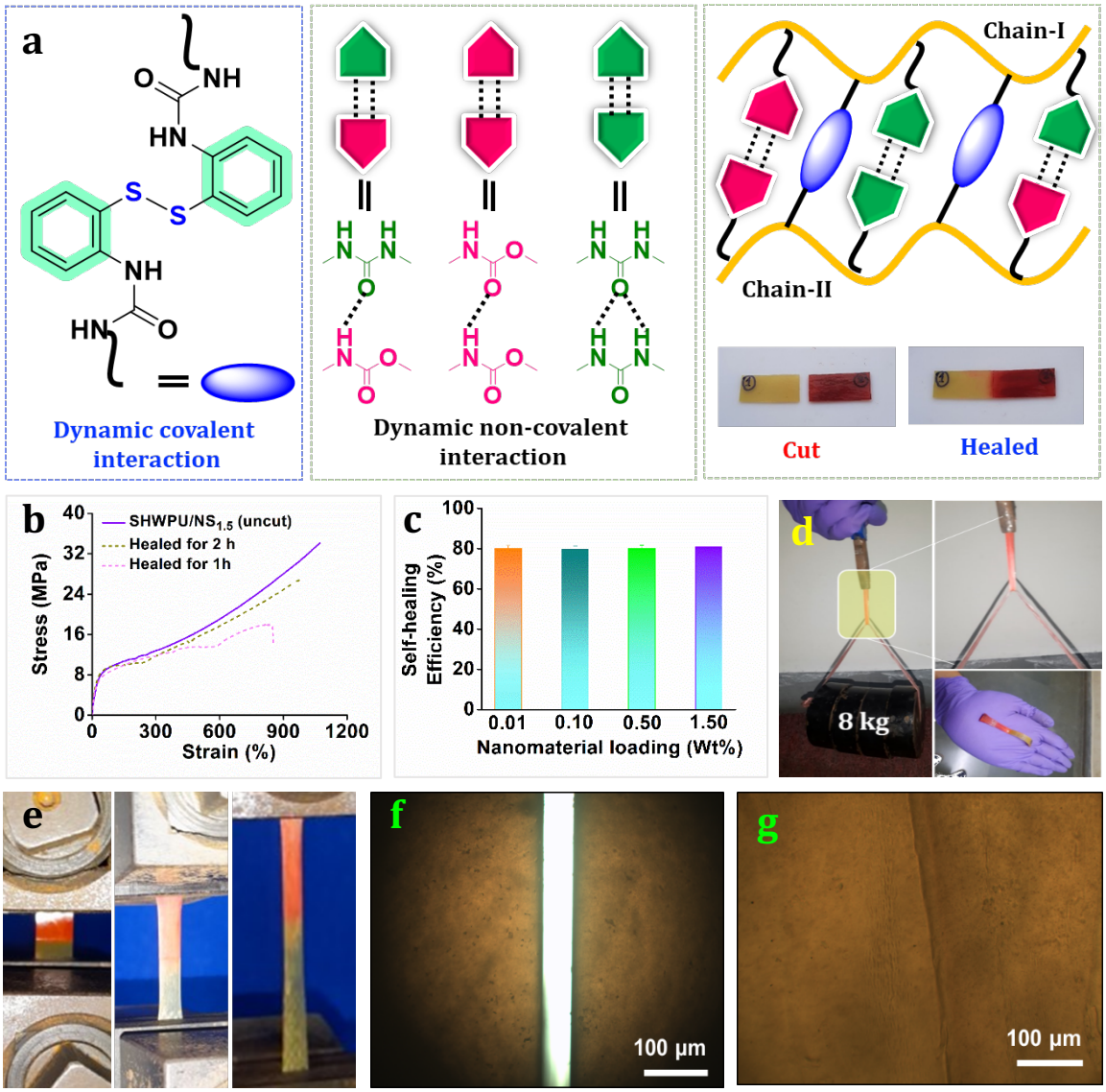

Figure 6.6. (a) Possible reversible dynamic interactions and healing mechanism, (b) stress-strain profiles of SHWPU/$NS_{1.5}$ film before and after healed at 110±5 °C for 1h and 2h using approximately 0.2 µL of DMF, (c) SH efficiency (%) of SHWPU/NS nanocomposite films, (d) weightlifting test (8 kg), (e) stretching test, after healing, and (f-g) optical microscopic images of cut and healed film (SHWPU/$NS_{1.5}$ film) (scale: 100 µm).

SH ability of the nanocomposite films was evaluated both quantitatively and qualitatively, as previously discussed. Each film was cut into two pieces and re-connected carefully using a trace amount of solvent (0.1-0.2 µL of DMF) and heated the same at 110±5 °C for different times. It has been observed that a SHWPU/$NS_{1.5}$ exhibits a maximum SH efficiency of 80.79% within 2 h (**Figure 6.6. (b)**). In particular, 2-APDS (S-S metathesis) and asymmetric IPDI-IPDA moieties (multiple hierarchical H-bonding) triggered the SH ability. Notably, the introduction of Mo@S-CN nanohybrid does indeed moderately reduce the self-

healing efficiency, primarily because of the distinctive lamellar structure of the nanohybrid, which, in turn, contributes to the enhancement of mechanical robustness [29]. Xu et al. also found a similar result for g-C_3N_4 nanosheets embedded in anticorrosive PU/g-C_3N_4 nanocomposite films [30]. It is pertinent to note that several reversible interactions play a role in the healing process. However, the lamellar structure containing nanosheets and nanorods restricts the mobility of polymeric chains, leading to the absence of a notable improvement in SH efficiency. Nevertheless, the utilization of a minute amount of solvent significantly aids in SH by enhancing chain mobility (**Figure 6.6. (c)**).

Moreover, the qualitative assessment of the SH capability of SHWPU/NS film was conducted through weight-lifting and stretching tests, as illustrated in **Figure 6.6 (d)** and **(e)**. Like unmodified SHWPU film, a representative healed SHWPU/$NS_{1.5}$ film (length 60 mm × width 5 mm × thickness 0.68 mm) can lift a load of 8 kg with minor damage and can be stretched up to twice its original length. Again, optical microscopic images (**Figure 6.6. (f)** and **(g)** demonstrated the cut and healed area of the SHWPU/$NS_{1.5}$ film. these results support the retention of good healing efficiency.

6.3.6. Hemocompatibility assay

Clinically relevant implantable materials that come in close contact with the variety of vasculature in vivo need to be evaluated for their hemocompatibility. This can be done by virtue of platelet adhesion and activation characteristics and the hemolytic assessment of the material. The requisite of minimal platelet adhesion and activation as well as minimal hemolysis is an essential criterion for synthetic biomaterials that could be used in the vicinity of blood. Here the SHWPU/$NS_{1.5}$ discs and Mo@S-CN nanohybrid suspension coated surfaces were assessed for these properties. It was observed that both SHWPU/$NS_{1.5}$ discs and bare Mo@S-CN nanohybrid suspension coating could retain the visibly meagre number of platelets on their surfaces as compared to the positive control, i.e., collagen-coated surfaces (**Figure 6.7. (a**)). However, the suspension-coated surface yielded greater platelet adhesion as compared to the SHWPU/$NS_{1.5}$ discs. The LDH activity corroborates these findings and we found that the platelet activity of both SHWPU/$NS_{1.5}$ discs and Mo@S-CN nanohybrid suspension-coated surfaces was significantly lower than the control and the SHWPU/$NS_{1.5}$ discs showed lesser platelet activity than Mo@S-CN nanohybrid suspension coated surfaces (**Figure 6.7. (b)**). These findings are in concomitance with our previous results of SHWPU discs [31-35]. Both SHWPU/$NS_{1.5}$ discs and Mo@S-CN nanohybrid suspension coated

surfaces could be considered anti-thrombogenic, and an in vivo evaluation of the same is presented.

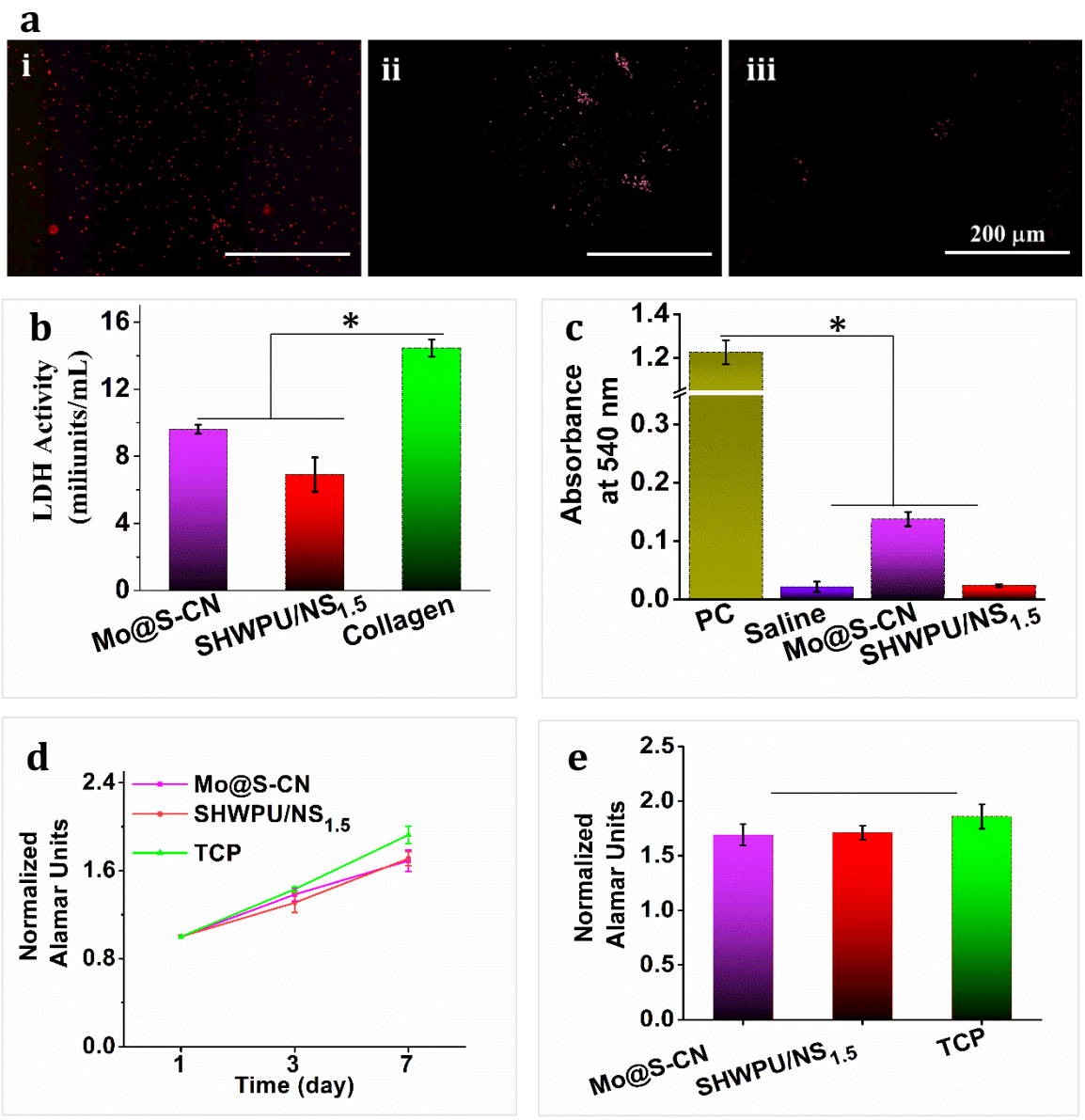

Figure 6.7. (a) Representative phalloidin stained micrographs of platelets adhered to (i) collagen, (ii) Mo@S-CN nanohybrid suspension coated surfaces, and (iii) SHWPU/$NS_{1.5}$ disc. (scale bar: 200 µm), (b) LDH activity of platelets adhered to collagen, S SHWPU/$NS_{1.5}$ disc and Mo@S-CN nanohybrid coated surfaces, (c) RBC lysis denoted by the absorbance in the presence of Triton-X100 (PC), saline, Mo@S-CN nanohybrid coated surfaces and SHWPU/$NS_{1.5}$ discs, (d) Alamar based cellular proliferation on day 1, 3 and 7, and (e) alamar based proliferation index on day 7 for TCP, Mo@S-CN nanohybrid coated surfaces and SHWPU/$NS_{1.5}$ discs. (n=3, #p≤0.001, *p≤0.05).

The haemolytic/ RBC lysis assay yielded similar results as the SHWPU/$NS_{1.5}$ discs and Mo@S-CN nanohybrid suspension-coated surfaces both showed significantly lower ($p \leq 0.01$) RBC lysis than the positive control and comparable to the saline (**Figure 6.7. (c)**). In tandem with the previous observation, the SHWPU/$NS_{1.5}$ discs showed considerably lower RBC lysis as compared with the Mo@S-CN nanohybrid suspension-coated surfaces. This

might be attributed to the particulate nature and leaching of the coating. These findings indicate the applicability of the developed suspension and the SHWPU films in environments where they might come in contact with blood such as stents, conduits, suture materials, and implants.

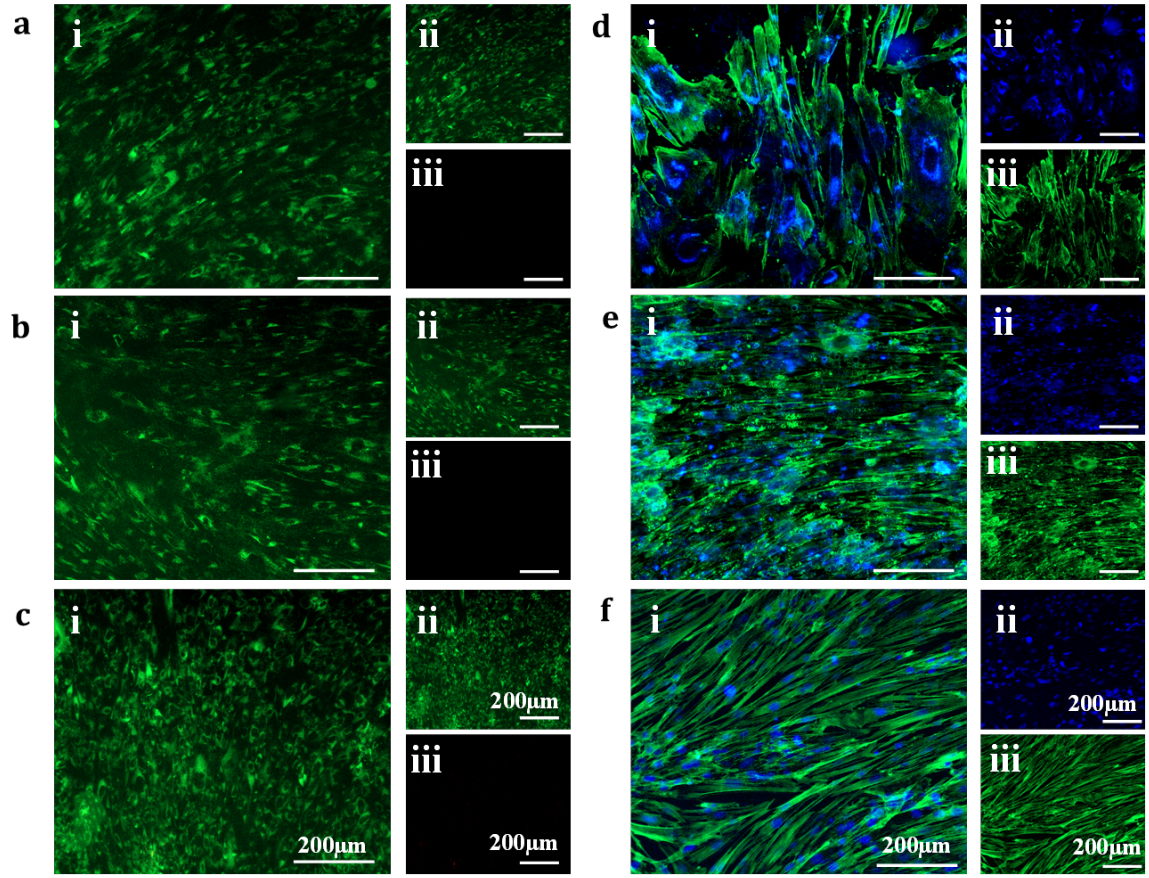

Figure 6.8. Representative live-dead stained micrographs of human dermal fibroblasts on day 7 when cultured on (a) Mo@S-CN nanohybrid coated surfaces, (b) SHWPU/NS-1.5 and (c) 2D control tissue culture dishes. (i) Merged image, (ii) represent the live (green channel) cells and (iii) represent the dead (red channel) cells. Representative phalloidin-DAPI stained micrographs of human dermal fibroblasts on day 7 when cultured on (d) Mo@S-CN nanohybrid coated surfaces, (e) SHWPU/NS-1.5, and (f) 2D control tissue culture dishes. (i) Show merged images, (ii) represent the nucleus (blue channel) of the cells, and (iii) represent the cytoskeleton (green channel) of the cells.

6.3.7. *In vitro* cell viability and proliferation

Cellular viability and proliferation assays were conducted using fibroblasts as a model cell type for the Mo@S-CN nanohybrid coated surfaces and SHWPU/$NS_{1.5}$ S discs. Both the surfaces were found to be highly conducive for cellular attachment and proliferation as could be seen from the alamar blue reduction (**Figure 6.7 (d)** and **(e)**), live dead micrographs (**Figure 6.8 (a)** and **(b)**) and the phalloidin stained micrographs (**Figure 6.8 (d)** and **(e)**) as compared to the TCP control. The cells were found to proliferate with a similar proliferation index after 7 days as compared to the TCP control on both Mo@S-CN nanohybrid coated

surfaces and SHWPU/$NS_{1.5}$ discs. This could be directly correlated with cellular metabolic activity and hence their proliferation [34]. HDFs proliferated >1.5 times when seeded on both Mo@S-CN-NS coated surfaces and SHWPU/$NS_{1.5}$ discs which was comparable to the proliferation index of TCP (~1.8 times). No significant difference was observed between all the groups after 7 days (**Figure 6.8 (e)**). Also, the viability and morphology of HDFs seeded on both Mo@S-CN nanohybrid coated surfaces and SHWPU/$NS_{1.5}$ discs were found to be comparable with the spread morphology of the TCP control (**Figure 6.8 (e)** and **(f)**) after 7 days of incubation. HDFs were found to possess spread morphology and were found to grow in a similar fashion as compared to the TCP. Both Mo@S-CN nanohybrid coated surfaces and SHWPU/$NS_{1.5}$ discs showed excellent cellular viability, proliferation as well as cellular morphology when compared to the tissue culture plates over the period of 7 days. Further, these materials need to be tested in vivo for their compatibility as implantable materials.

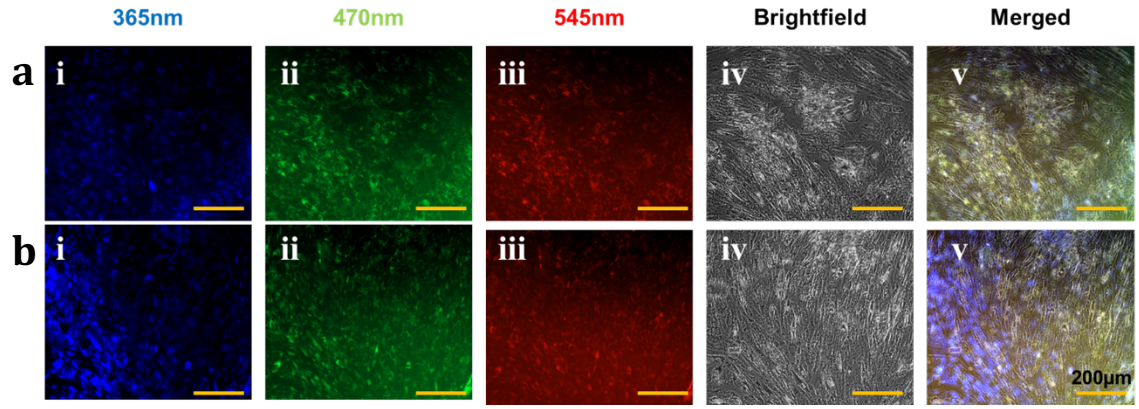

Figure 6.9. (a) and (b) Representative unstained micrographs of human dermal fibroblasts under various excitations; (i) 365 nm excitation, (ii) 470 nm excitation, (iii) 545 nm excitation, (iv) brightfield images, and (v) merged images.

6.3.8. *In vitro* fluorescence tagging, bio-imaging, and anti-counterfeiting applications

Mo@S-CN nanohybrid coated surfaces showed excellent cellular viability, proliferation, and cellular morphology, hence Mo@S-CN nanohybrid was further used for the evaluation of potential tagging and bio-imaging applications. The cells cultured on the coverslips and treated with the Mo@S-CN nanohybrid were exposed to the excitation wavelengths of 365 nm, 470 nm, and 545 nm and their fluorescence was recorded via microscope. The cells were found to show fluorescence in all the channels with variable intensity as could be seen from the two different fields from cultures of HDFs treated with the Mo@S-CN nanohybrid for 72 h. Blue emission from 365 nm excitation (**Figure 6.9 (a)-i** and **(b)-i**), green emission from 470 nm excitation (**Figure 6.9 (a)-ii** and **(b)-ii**) and red emission from 545 nm excitation (**Figure 6.9 (a)-iii** and **(b)-iii**) were detected and colocalized with the cells in brightfield images (**Figure 6.9 (a)-iv** and **(b)-iv**) and merged to represent the same (**Figure 6.9 (a)-v**

and **(b)-v**). The potential internalization of the Mo@S-CN nanohybrid could be attributed to the fluorescence detected from the cells. This could be further investigated for imaging in different in vitro and in vivo conditions.

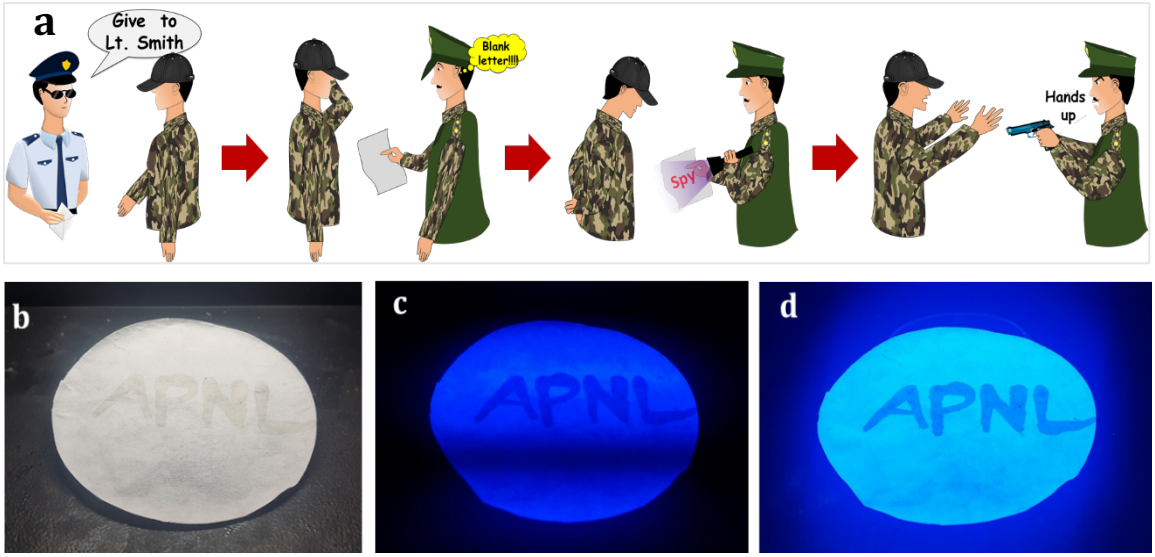

Figure 6.10. (a) Encryption application of the luminescent image in the virtual military scenario, the appearance of the word "APNL" written by using SHWPU/$NS_{1.5}$ dispersions in the presence of (b) white light, (c) UV-365 nm, and (d) UV-254 nm light.

Again, **i**nspired by the bright cyan PL feature and biocompatibility nature of SHWPU/$NS_{1.5}$ dispersion, the luminescent image can be used as an anti-counterfeiting tool. **Figure 6.10 (a)** represents a virtual scenario of encryption of important information using PL active ink in a military application. To establish the performance of SHWPU/$NS_{1.5}$ dispersion as anti-counterfeiting ink, the word "**APNL**" was written on filter paper (pore size 20 μm). The word was nearly imperceptible to the naked eye in daylight, but it became readily visible when exposed to UV light at both 365 nm and 254 nm wavelengths. This ink could be further tested on various surfaces such as plastic, metal, wood, and so forth.

5.4 Conclusion

In conclusion, we have developed a series of photoluminescent SHWPU/NS nanocomposites using Mo@S-CN nanohybrid as the reinforcing agent in the SHWPU matrix. TEM images disclosed that the Mo@S-CN nanohybrid comprised of g-C_3N_4 nanosheet and MoO_x nanorod creating a complex lamellar structure. The SHWPU/NS nanocomposites showed loading-dependent improvement in mechanical properties, especially, in tensile strength, fracture energy, and thermal stability. Interestingly, the incorporation of Mo@S-CN nanohybrid not only advances the congenital properties of the parental SHWPU to a remarkable degree but also imparts fluorescence activity into the WPU matrix. Most importantly, the biocompatibility character of Mo@S-CN nanohybrid and SHWPU/NS nanocomposite was

verified by *in vitro* hemocompatibility study, *in vitro* cytocompatibility test, and cell proliferation assessment. Furthermore, the aqueous dispersion of Mo@S-CN nanohybrid and SHWPU/NS nanocomposite were tested for bioimaging and anti-counterfeiting applications. Hence, these materials possess generous promise and hold the potential to chart a novel path in the realm of advanced smart materials, suitable for a wide range of applications.

References

[1] Liu, J., Wang, H. and Antonietti, M. Graphitic carbon nitride "reloaded": emerging applications beyond (photo) catalysis. *Chemical Society Reviews*, 45(8):2308-2326, 2016.

[2] Xie, Y., Ye, M., Xiong, B., Liu, B., Liu, F., He, H., Yang, L., Jiang, L., Dan, Y. and Zhou, Y. Enhanced reactive-oxygen-species generation and photocatalytic efficiency with internal imide structures of different ratio in metal-free perylene-g-C_3N_4 semiconductors. *Applied Surface Science*, 546:149138, 2021.

[3] Schaber, P. M., Colson, J., Higgins, S., Thielen, D., Anspach, B. and Brauer, J. Thermal decomposition (pyrolysis) of urea in an open reaction vessel. *Thermochimica Acta*, 424(1-2):131-142, 2004.

[4] Li, K., He, Y., Chen, P., Wang, H., Sheng, J., Cui, W., Leng, G., Chu, Y., Wang, Z. and Dong, F. Theoretical design and experimental investigation on highly selective Pd particles decorated C_3N_4 for safe photocatalytic NO purification. *Journal of Hazardous Materials*, 392:122357, 2020.

[5] Wang, F., Yang, Z., Li, J., Zhang, C. and Sun, P. Bioinspired polyurethane using multifunctional block modules with synergistic dynamic bonds. *ACS Macro Letters*, 10(5):510-517, 2021.

[6] Deisingh, A. K. Pharmaceutical counterfeiting. *Analyst*, 130(3):271-279, 2005.

[7] Aldhous, P. Counterfeit pharmaceuticals: murder by medicine. *Nature*, *434*(7030):132-137, 2005.

[8] Bayan, R. and Karak, N. Photoluminescent oxygeneous-graphitic carbon nitride nanodot-incorporated bioderived hyperbranched polyurethane nanocomposite with anticounterfeiting attribute. *ACS Omega*, 4(5):9219-9227, 2019.

[9] You, R., Dou, H., Chen, L., Zheng, S. and Zhang, Y. Graphitic carbon nitride with S and O codoping for enhanced visible light photocatalytic performance. *RSC Advances*, 7(26):15842-15850, 2017.

[10] Jaysiva, G., Manavalan, S., Chen, S. M., Veerakumar, P., Keerthi, M. and Tu, H. S. MoN nanorod/sulfur-doped graphitic carbon nitride for electrochemical determination

of chloramphenicol. *ACS Sustainable Chemistry & Engineering*, 8(30):11088-11098, 2020.

[11] Zhang, X., Xie, X., Wang, H., Zhang, J., Pan, B. and Xie, Y. Enhanced photoresponsive ultrathin graphitic-phase C3N4 nanosheets for bioimaging. *Journal of the American Chemical Society*, 135(1):18-21, 2013.

[12] Bai, X., Li, M., Li, J., Rao, X., Zheng, S. and Zhang, Y. Graphitic carbon nitride codoped with sulfur and yttrium for efficient visible-light photocatalytic performance. *ACS Applied Energy Materials*, 4(12):14390-14399, 2021.

[13] Pan, D., Zhang, J., Li, Z., Wu, C., Yan, X. and Wu, M. Observation of pH-, solvent-, spin-, and excitation-dependent blue photoluminescence from carbon nanoparticles. *Chemical Communications*, 46(21):3681-3683, 2010.

[14] Pan, D., Zhang, J., Li, Z. and Wu, M. Hydrothermal route for cutting graphene sheets into blue-luminescent graphene quantum dots. *Advanced Materials*, 22(6):734-738, 2010.

[15] Zhai, L. F., Chen, Z. X., Qi, J. X. and Sun, M. Manganese-doped molybdenum oxide boosts catalytic performance of electrocatalytic wet air oxidation at ambient temperature. *Journal of Hazardous Materials*, 428:128245, 2022.

[16] Benyahya, S., Desroches, M., Auvergne, R., Carlotti, S., Caillol, S. and Boutevin, B. Synthesis of glycerin carbonate-based intermediates using thiol–ene chemistry and isocyanate free polyhydroxyurethanes therefrom. *Polymer Chemistry*, 2(11):2661-2667, 2011.

[17] Xu, L., Li, C. and Ng, K. S. In-situ monitoring of urethane formation by FTIR and Raman spectroscopy. *The Journal of Physical Chemistry A*, 104(17):3952-3957, 2000.

[18] Chen, M., Zhang, X., Luo, C., Qi, R., Peng, H. and Lin, H. Highly stable waterborne luminescent inks based on MAPbBr3@ PbBr (OH) nanocrystals for LEDs and anticounterfeit applications. *ACS Applied Materials & Interfaces*, 13(17):20622-20632, 2021.

[19] Allo, B. A., Rizkalla, A. S. and Mequanint, K. Synthesis and electrospinning of ε-polycaprolactone-bioactive glass hybrid biomaterials via a sol– gel process. *Langmuir*, 26(23):18340-18348, 2010.

[20] Javni, I., Petrović, Z. S., Guo, A. and Fuller, R. Thermal stability of polyurethanes based on vegetable oils. *Journal of Applied Polymer Science*, 77(8):1723-1734, 2000.

[21] Shikha, Meena, M., Jacob, J. and Nebhani, L. Phosphate-functionalized silica for improved flame retardancy and thermal stability of thermoplastic polyurethane. *ACS Applied Polymer Materials*, 4(9):6332-6341, 2022.

[22] Zhu, J., Xiao, P., Li, H. and Carabineiro, S. A. Graphitic carbon nitride: synthesis, properties, and applications in catalysis. *ACS Applied Materials & Interfaces*, 6(19):16449-16465, 2014.

[23] Gaddam, S. K., Pothu, R. and Boddula, R. Graphitic carbon nitride (g-C_3N_4) reinforced polymer nanocomposite systems—A review. *Polymer Composites*, 41(2):430-442, 2020.

[24] Lu, H. F., Wang, M., Chen, X. M., Lin, B. P. and Yang, H. Interpenetrating liquid-crystal polyurethane/polyacrylate elastomer with ultrastrong mechanical property. *Journal of the American Chemical Society*, 141(36):14364-14369, 2019.

[25] Shi, Y., Yu, B., Zhou, K., Yuen, R.K., Gui, Z., Hu, Y. and Jiang, S. Novel $CuCo_2O_4$/graphitic carbon nitride nanohybrids: Highly effective catalysts for reducing CO generation and fire hazards of thermoplastic polyurethane nanocomposites. *Journal of hazardous materials*, 293:87-96, 2015.

[26] Mu, C., Ren, J., Chen, H., Wu, Y., Xu, Q., Sun, X. and Yan, K. Graphitic carbon nitride/zeolitic imidazolate framework-8 nanoparticles with antibacterial properties for textile coating. *ACS Applied Nano Materials*, 4(10):10634-10644, 2021.

[27] Greensmith, H. W. Rupture of rubber. X. The change in stored energy on making a small cut in a test piece held in simple extension. *Journal of Applied Polymer Science*, 7(3):993-1002, 1963.

[28] Zhang, L., Liu, Z., Wu, X., Guan, Q., Chen, S., Sun, L., Guo, Y., Wang, S., Song, J., Jeffries, E. M. and He, C. A highly efficient self-healing elastomer with unprecedented mechanical properties. *Advanced Materials*, 31(23):1901402, 2019.

[29] Xu, J., Li, Y., Liu, T., Wang, D., Sun, F., Hu, P., Wang, L., Chen, J., Wang, X., Yao, B. and Fu, J. Room-temperature self-healing soft composite network with unprecedented crack propagation resistance enabled by a supramolecular assembled lamellar structure. *Advanced Materials*, 35: 2300937, 2023.

[30] Xu, J. H., Ye, S., Di Ding, C., Tan, L. H. and Fu, J. J. Autonomous self-healing supramolecular elastomer reinforced and toughened by graphitic carbon nitride nanosheets tailored for smart anticorrosion coating applications. *Journal of Materials Chemistry A*, 6(14);5887-5898, 2018.

[31] Duarah, R., Singh, Y. P., Gupta, P., Mandal, B. B. and Karak, N. High performance bio-based hyperbranched polyurethane/carbon dot-silver nanocomposite: a rapid self-expandable stent. *Biofabrication*, 8(4):045013, 2016.

[32] Duarah, R., Singh, Y. P., Gupta, P., Mandal, B. B. and Karak, N. Smart self-tightening surgical suture from a tough bio-based hyperbranched polyurethane/reduced carbon dot nanocomposite. *Biomedical Materials*, 13(4):045004, 2018.

[33] Morang, S., Bandyopadhyay, A., Rajput, J. H., Mandal, B. B., Poundarik, A. and Karak, N. Robust self-healable and three-dimensional printable thermoplastic elastomeric waterborne polyurethane for artificial muscle and biomedical scaffold applications. *ACS Applied Polymer Materials*, 5(10):8518–8532, 2023.

[34] Morang, S., Bandyopadhyay, A., Mandal, B. B. and Karak, N. Asymmetric hard domain-induced robust resilient biocompatible self-healable waterborne polyurethane for biomedical applications. *ACS Applied Bio Materials*, 6(7):2771-2784, 2023.